A Broadband Metasurface Luneburg Lens for Microwave Surface Waves

Julia D. de Pineda,[a] Rhiannon C. Mitchell-Thomas, Alastair P. Hibbins, and J. Roy Sambles
Electromagnetic and Acoustic Materials Group, Department of Physics and Astronomy, University of Exeter, Stocker Road, Exeter EX4 4QL, United Kingdom

(Dated: 23 November 2017)

A broadband planar microwave Luneburg lens made of a three-layer metasurface with hexagonal symmetry is presented. This metasurface supports a transverse-electric mode confined to the surface that presents very low dispersion and a stable mode index across a broad frequency band. This enables the lens to operate in the range of frequencies between 8 GHz and 19 GHz. The lens was manufactured using a lithographic technique with three 25 µm copper-coated Mylar sheets. The resulting device is only 75 µm thick, flexible and light-weight.

Microwave metasurfaces are typically single or few-layer structures comprised of non-diffracting arrays of subwavelength sized elements whose properties are determined by the geometry and arrangement of these elements. Metasurfaces and their ability to manipulate electromagnetic fields have been studied for a number of applications including mimicking surface plasmons in the microwave regime,[1] and guiding surface waves to transform them into different wavefield configurations with desirable properties.[2] The ability to control the propagation of surface waves that can be achieved by the use of metasurfaces, in addition to the fact that they are cheap, easy to fabricate, lightweight, and thin make them ideal for the manufacturing of low profile microwave devices such as lenses[3] and leaky-wave antennas suitable for telecommunications, space or defence applications.[4]

One example of these microwave devices is the Luneburg lens.[5] Such a lens is a spherical device (or circular in the case of surface waves) that can focus the radiation of a point source placed on its perimeter to create a plane wave on the opposite side of the lens or vice versa. This effect is achieved by a graded mode index profile that decreases radially from the center of the lens. These devices work under the assumption that the ray optics approximation can be applied.

Luneburg lenses have been implemented in many ways over the past 50 years. A Luneburg lens for transverse magnetic (TM) surface-waves was theoretically proposed in 1944 and a working device was first developed in 1960.[6] In that case the mode index profile was achieved by the superposition of layers of dielectric materials with the appropriate permittivity, resulting in bulky devices. In 2001, Park et al.[7] developed a planar Luneburg lens for TM surface waves comprised of a square array of square posts of varying height in a parallel-plate waveguide. A surface wave Luneburg lens has also been proposed and characterized for transverse electric (TE) surface waves,[8] in which three concentric rings of circular holes of different sizes are etched in a square lattice on the top plate of a dielectric-filled parallel metal plates waveguide, providing the required mode index profile. In all cases, the graded index profile is achieved by varying the mode index in steps rather than as a continuous function of the radius due to fabrication limitations. However, this approximation has proven to be valid, enabling a satisfactory performance of the device.

Metasurfaces have proven to be a good way of improving the profile of microwave devices, allowing thinner and lighter planar designs. However, they usually present a limitation in bandwidth due to the highly dispersive behaviour of the surface modes they support[9] and this limitation grows as the required range of variation of the mode index increases. Different methods to increase the bandwidth have been proposed. In 2010 Pfeiffer and Grbic proposed a printed Luneburg lens antenna based on a combination of meandering crossed microstrip lines that improved the bandwidth with respect to other metamaterial Luneburg lenses.[10] It has also been found that a significant improvement in bandwidth and also an increase of mode index can be achieved by the superposition of two mirrored metasurfaces that are displaced by exactly half a unit cell. This symmetry operation is known as glide symmetry.[11–14]

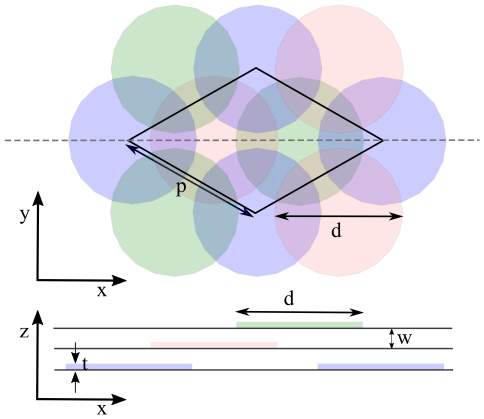

FIG. 1. Unit cell of the three-layer metasurface. Each layer is represented by a different colour. They comprise of circular patches with a diameter of 2.15 mm on a hexagonal lattice with periodicity $p = 2.4$ mm. Each layer is shifted $\frac{p}{\sqrt{3}}$ in the x-direction with respect to the previous one. The layers are separated by a 25 µm dielectric slab with relative permittivity $\varepsilon = 2.8$.

[a] Electronic mail: jd602@exeter.ac.uk

In this work, we present a different way of improving the bandwidth. By means of the implementation of a metasurface comprised of three layers of metallic circular patches arranged in a hexagonal lattice, we exploit an enhanced mode index, achieved by the overlapping of the metal layers, with the linearising of the dispersion of the modes caused by the degeneracy of the first two modes in the K point of the Brillouin zone, typical of some structures with hexagonal symmetry.[15] Because of this degeneracy, the modes are propagating at the K-point of the Brillouin zone boundary instead of forming a standing wave. As the group velocity here is nonzero, the curvature of the mode is reduced and therefore the mode is less dispersive.

The metallic patches are printed on 25 µm Mylar sheets with a relative permittivity $\varepsilon = 2.8$, and this dielectric acts as a spacing between the different layers of patches. The dielectric sheet is chosen to be very thin in order to maximize the confinement of the field to the overlap regions between the layers of patches.[16] Each layer is displaced by $\frac{p}{\sqrt{3}}$ in the x-direction, where p is the pitch of the structure and also the distance between the centres of two adjacent patches. In this way the complete three-layer structure forms an ABC hexagonal 3D lattice. A unit cell of the structure is shown in Fig.1, where a pitch $p = 2.4\,\text{mm}$ and a patch diameter $d = 2.15\,\text{mm}$ were chosen. These parameters can be varied depending on the desired range of frequencies of operation. The proposed metasurface was characterized in the first instance by calculating its eigenmodes using a commercial finite element method (FEM) modelling software[17] and secondly by experimentally determining its dispersion via near-field measurements.

Using a FEM solver, the dispersion relation for the lower modes of the three-layer structure and the isofrequency contours, in reciprocal space, were found as well as the modes' field distribution. The isofrequency contours, plotted in Fig. 2, are a measure of the isotropy of the surface mode propagation. They remain nearly circular for frequencies up to 22 GHz, however, for higher frequencies some distortion is observed, which implies that the surface is no longer isotropic as the wave vector has now become direction-dependent.

For this kind of structure the mode index is not a property of the bulk material but a way of specifying how much the mode deviates from the light line, and hence, the phase velocity of the mode. It is defined as the ratio between the wave vector of the mode and that of the light line for a given frequency and it is related to the phase velocity as $n_m = \frac{c}{v_{phase}}$. In Fig. 3, the variation of the mode index, obtained from the simulation data, for the lower mode supported by the metasurface is presented. It is of the order of 2.4 for the considered patch diameter of $d = 2.15\,\text{mm}$ and only varies by ±5% over the range of frequencies between 9 GHz and 21 GHz. In addition, the difference in index across this frequency range for the Γ to M and K to Γ directions is negligible, confirming the isotropic nature of the supported surface wave dispersion.

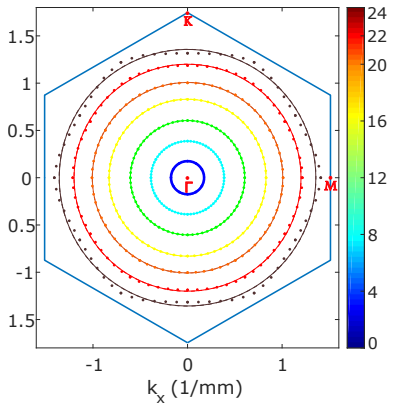

FIG. 2. Modelled isofrequency contours for the three-layer metasurface (dots). Each set of points is accompanied by a fitted circle (solid line). The Brillouin zone and the Γ, M and K points are also represented. This graph has been plotted with the simulation data from the FEM solver for a patch size $d = 2.15\,\text{mm}$

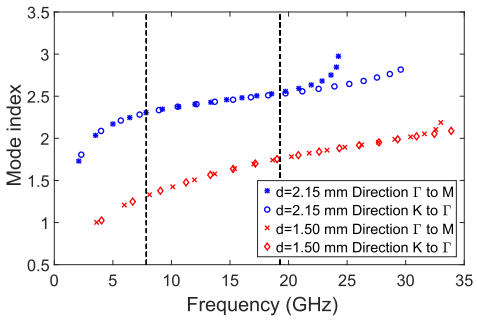

FIG. 3. Frequency dependence of the mode index for the lowest mode supported by the metasurface. The blue markers correspond to patches of 2.15 mm and the red markers correspond to a smaller patch diameter $d = 1.50\,\text{mm}$, the smallest patch size used in the luneburg lens design. The range over which the mode index for the bigger patch size metasurface varies by ±5% is denoted by the dotted lines.

Further simulations, in which the patch diameter is varied while the pitch is kept constant demonstrate that it is possible to vary the phase velocity and thus the mode index of the metasurface. As the size of the patches is increased, the confinement of the mode to the surface is improved and therefore the resulting metasurface possesses a higher mode index. For the considered pitch $p = 2.4\,\text{mm}$, it is possible to achieve a range of variation for the mode index between 1.15 and 2.5 while conserving the isotropy of the surface when the diameter of the patches is varied between 1.30 mm, where there is no overlap between the patches of two different layers, and 2.35 mm. This provides not only a simple way of defining a graded mode index across the surface but also a way of implementing a modulated surface impedance and therefore the possibility of transforming the bounded surface waves into leaky waves,[18] extending the range of appli-

cations for this also to the manufacturing of leaky-wave antennas.[19] The frequency dependence of the mode index for a metasurface with a smaller patch size is also included (red markers) in Fig. 3. In particular, it corresponds to the smallest patch size used in the lens design.

Using a lithographic technique the metasurface described in Fig. 1 was fabricated. It was chosen to have a uniform patch size ($d = 2.15\,\text{mm}$) across the entire sample. The pattern was printed onto three copper coated Mylar sheets (with a 25 µm Mylar layer) and chemically etched to leave the desired circular patch pattern. To obtain the dispersion, the amplitude and phase of the field were measured for 351 frequencies between 5 GHz and 40 GHz. The studied metasurface supports a TE-like surface mode. The electric field is transverse to the propagation direction, confined inside the dielectric, while the magnetic field has a component parallel to the direction of propagation. A pair of loop antennas were used as a source and probe to excite and measure the field propagating across the surface. Both antennas were oriented so that the loop was in the plane of the surface and they were placed approximately 0.5 mm away from the sample. This configuration maximizes the detection of the out-of-plane magnetic field. The source was placed in the center of the sample, and the probe was used to scan an area of 200 mm by 200 mm on the opposite face of the sample.

Both coaxial cables were connected to a VNA that measures the amplitude of the field and the phase difference between the detected signal and an internal reference signal. Hence, the instantaneous field map of the mode propagating across the surface is obtained. Finally, a fast Fourier transform was performed to obtain the isofrequency contours of each frequency in reciprocal space and hence the dispersion diagram. As shown in Fig. 4 for the uniformly patterned metasurface, an excellent agreement between the simulation results and the experimental data is obtained.

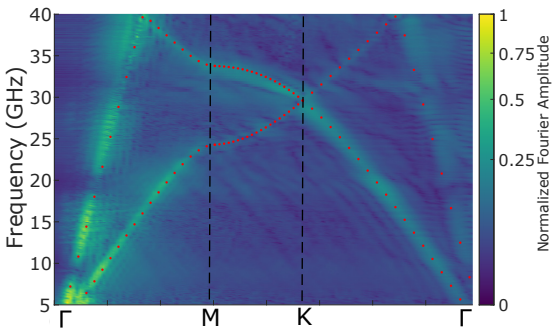

FIG. 4. Experimental dispersion for the three-layer metasurface described in Fig 1. The red dots represent the modelled dispersion, showing great agreement between the experimental and simulation data.

The Luneburg lens was printed using the lithographic technique described before. Since we seek a surface-wave device, the sample must support a surface wave beyond the lens (radius R) itself. We therefore design a sample with a background mode index $n_0 = 1.6$ which yields a surface-wave wavelength of $\lambda_0 = 1.25\,\text{mm}$ at 15 GHz. To implement the lens, the patch size of every unit cell that comprises the structure is tailored to give the required mode index according to,[5]

$$n_m(r) = \begin{cases} n_0 & \text{if } r > R_0 \\ n_0\sqrt{2 - \left(\frac{r}{R}\right)^2} & \text{if } r \leq R_0 \end{cases} \quad (1)$$

where R_0 is the radius of the lens and r is the radial distance to its center. The diameter of the lens was chosen to be 135 mm, which is of the order of 10 wavelengths, so that the geometrical optics approximation can be applied.

It is to be noted that a local periodicity was assumed to calculate the mode index for each value of patch size although each element is surrounded by nonidentical neighbours. With this assumption, the size of each patch is determined by its distance to the center of the lens (r). From equation (2) it is possible to determine the mode index that corresponds to each element depending on its position and the required patch size can be extrapolated from the curve illustrated in Fig 5, obtained using simulation data.

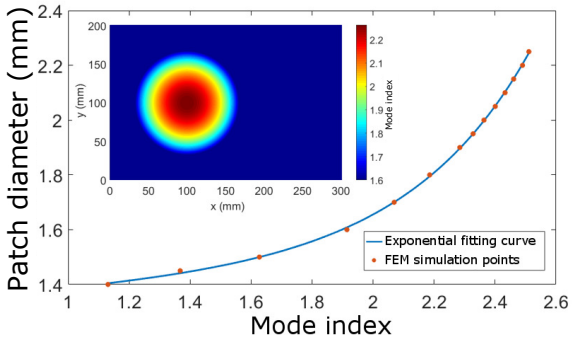

FIG. 5. Relationship between the patch diameter and the achieved mode index of the surface at the design frequency of 15 GHz. Inset: Mode index profile of the designed Luneburg lens.

The experimental setup described before was also used to measure the fields propagating across the lens. In this case, the source was placed at the focus of the Luneburg lens, located on its perimeter, and the probe was used to scan an area of 200 mm by 300 mm on the opposite face of the sample.

The measured field is the external exponentially decaying field. This field is quite weak as the fields that propagate across the surface are strongly confined to the dielectric spacing between the layers, where it is not possible to measure. As a consequence, the measured surface wave is masked by free space radiation, also detected by the antenna. To overcome this, a 2D fast Fourier transform was applied to the measured fields. In this way, it is possible to separate in wave vector (k) the bound

surface mode from the free space radiation. As is shown in Fig. 4, the modes bound to the surface have higher momentum and therefore it is a simple matter to remove the radiative part. The field plots of the modes bound to the surface are obtained after applying an inverse 2D Fourier transform to the post-processed data. These are plotted in Fig. 6 (left column) at 16 GHz as well as for the limit frequencies of the operational bandwidth. For all frequencies between 8 GHz and 19 GHz the circular wavefronts from the point source are transformed into plane waves after propagating across the lens, with a fractional frequency bandwidth of 73%.

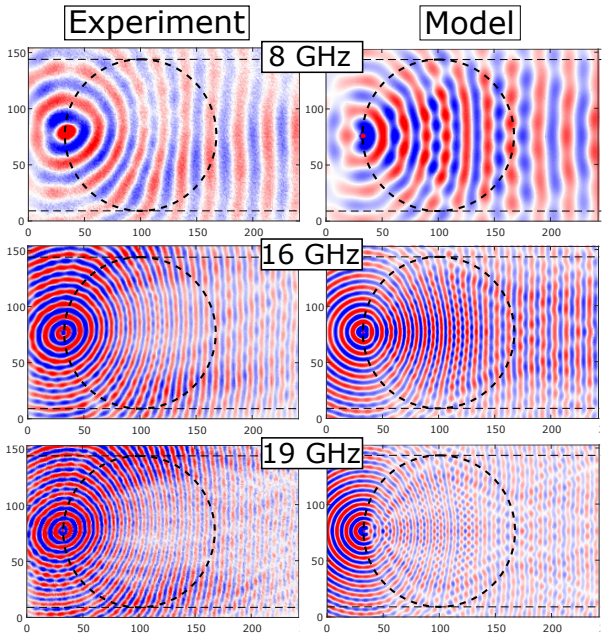

FIG. 6. Instantaneous field plot across the surface for 8 GHz, 16 GHz and 19 GHz. The perimeter of the lens is shown with a dashed line. The source is placed at the focus of the lens (located on its perimeter). The surface waves exit the lens to the right with planar wavefronts. The left column corresponds to the experimental results and the right column to the fields obtained in the FEM simulation (Out-of-plane H magnetic field).

In Fig. 6, (right column) the field distribution of the surface wave for each frequency are compared with the results of a FEM simulations where the entire surface has been modelled as a varying impedance sheet. The impedance boundary condition allows one to define a mode index profile that does not vary with frequency. The surface impedance is given as $Z_s = R - i\chi$, where R is the reactance and χ is the inductance. The impedance, for TE surface waves is related to the mode index by the following expression[20]

$$\chi = \frac{1}{\sqrt{n_m^2 - 1}}. \qquad (2)$$

Both, the experiment and the model show similar behaviour: the wavelength of the surface wave is reduced as it gets closer to the centre of the lens due to the increase in mode index, and the wavefronts are planar on exiting the lens. While the agreement is good, the experimental measurement displays some distortion of the spherical wave fronts, probably due to a small misalignment of the three layers which increases the overlap regions between the patches in one direction and decreases them in other directions, causing an undesired anisotropy of the index profile. The experimental data is also affected by some interference produced by the wave reflection at the edge of the sample.

We acknowledge financial support from the Engineering and Physical Sciences Research Council (EPSRC) of the United Kingdom, via the EPSRC Centre for Doctoral Training in Metamaterials (Grant No. EP/L015331/1). All data created during this research are openly available from the University of Exeter's institutional repository at https://ore.exeter.ac.uk/repository/

[1] J. B. Pendry, L. Martín-Moreno, and F. J. García-Vidal, Science **305**, 847 (2004).
[2] S. Maci, G. Minatti, M. Casaletti, and M. Bosiljevac, IEEE Antennas and Wireless Propagation Letters **10**, 1499 (2011).
[3] M. Bosiljevac, M. Casaletti, F. Caminita, Z. Sipus, and S. Maci, IEEE Transactions on Antennas and Propagation **60**, 4065 (2012).
[4] G. Minatti, F. Caminita, M. Casaletti, and S. Maci, IEEE Transactions on Antennas and Propagation **59**, 4436 (2011).
[5] R. Luneburg, *The Mathematical Theory of Optics* (McGraw-Hill Book Company, University of California Press, Berkeley, 1964).
[6] C. H. Walter, IRE Transactions on Antennas Propagation **AP-8**, 508 (1960).
[7] Y.-j. Park, S. Member, A. Herschlein, and W. Wiesbeck, Transactions on Microwave Theory and Techniques **49**, 1854 (2001).
[8] L. Xue and V. F. Fusco, Microwave and Optical Technology Letters **50**, 378 (2008).
[9] J. A. Dockrey, M. J. Lockyear, S. J. Berry, S. A. R. Horsley, J. R. Sambles, and A. P. Hibbins, Physical Review B **87**, 1 (2013).
[10] C. Pfeiffer and A. Grbic, IEEE Transactions on Antennas and Propagation **58**, 3055 (2010).
[11] O. Quevedo-teruel, M. Ebrahimpouri, and M. N. M. Kehn, IEEE Antennas and Wireless Propagation Letters **15**, 484 (2016).
[12] M. Camacho, R. C. Mitchell-Thomas, A. P. Hibbins, J. R. Sambles, and O. Quevedo-Teruel, Opt. Lett. **42**, 3375 (2017).
[13] M. Ebrahimpouri, O. Quevedo-teruel, and E. Rajo-Iglesias, IEEE Microwave and Wireless Components Letters **27**, 542 (2017).
[14] R. C. Mitchell-Thomas, J. R. Sambles, and A. P. Hibbins, 11th European Conference on Antennas and Propagation (EUCAP) , 1396 (2017).
[15] M. Plihal and A. A. Maradudin, Physical Review B **44**, 8565 (1991).
[16] J. D. De Pineda, A. P. Hibbins, and J. R. Sambles, IEEE International Symposium on Antennas and Propagation USNC/URSI National Radio Science Meeting, 2017 , 831 (2017).
[17] COMSOL, Inc, "Comsol multiphysics,".
[18] A. A. Oliner and A. Hessel, IRE Transactions on Antennas and Propagation **7**, 201 (1959).
[19] G. Minatti, F. Caminita, E. Martini, S. Member, and S. Maci, IEEE Transactions on Antennas and Propagation **64**, 3896 (2016).
[20] D. Sievenpiper, L. Zhang, R. F. J. Broas, and E. Yablonovitch, IEEE Transactions on Microwave Theory and Techniques **47**, 2059 (1999).